ELSEVIER

Disturbances from Single Event Upsets in the GRACE Follow-On Laser Ranging Interferometer

Malte Misfeldt[a,b,*], Pallavi Bekal[a,b], Vitali Müller[a,b], Gerhard Heinzel[a,b]

[a]*Max-Planck Institute for Gravitational Physics, Callinstraße 38, 30167 Hannover, Germany*
[b]*Institut für Gravitationsphysik, Leibniz Universität Hannover, Callinstraße 38, 30167 Hannover, Germany*

Abstract

The Gravity Recovery And Climate Experiment – Follow On (GRACE-FO) satellite mission (2018-now) hosts the novel Laser Ranging Interferometer (LRI), a technology demonstrator for proving the feasibility of laser interferometry for inter-satellite ranging measurements. The GRACE-FO mission extends the valuable climate data record of changing mass distribution in the system Earth, which was started by the original GRACE mission (2002-2017). The mass distribution can be deduced from observing changes in the distance of two low-earth orbiters employing interferometry of electromagnetic waves in the K-Band for the conventional K-Band Ranging (KBR) and in near-infrared for the novel LRI.

This paper identifies possible radiation-induced Single Event Upset (SEU) events in the LRI phase measurement. We simulate the phase data processing within the Laser Ranging Processor (LRP) and use a template-based fitting approach to determine the parameters of the SEU and subtract the events from the ranging data. Over four years of LRI data, 29 of such events were identified and characterized.
© 2023 COSPAR. Published by Elsevier Ltd All rights reserved.

Keywords: GRACE-FO; Laser Ranging Interferometer; LRI; Single Event Upset; Bitflip; Cosmic Radiation

1. Introduction

The ongoing Gravity Recovery And Climate Experiment – Follow On (GRACE-FO) space mission consists of two nearly identical formation-flying satellites, launched on May 22nd, 2018 (Kornfeld et al., 2019). The objective of GRACE-FO and its predecessor GRACE (2002-2017) is to study mass redistribution within the Earth system by observing the differential gravimetric pull on the satellites (Wahr et al., 1998). Both satellites share a similar polar orbit at an altitude of about 490 km and an along-track separation of 220 ± 50 km (Wahr et al., 2004; Kornfeld et al., 2019).

The GRACE-FO twin satellites host the K-Band Ranging (KBR; or Microwave Instrument, MWI) and the Laser Ranging Interferometer (LRI) for precisely measuring the inter-satellite distance variations (Kornfeld et al., 2019). The conventional KBR, which is the primary ranging instrument, can resolve the inter-satellite distance variations with a noise level of about $1\,\mu m/\sqrt{Hz}$ at Fourier frequencies of 1 Hz (Kornfeld et al., 2019). The LRI, a technology demonstrator, uses heterodyne near-infrared laser interferometry for the ranging measurement (Sheard et al., 2012). It has been and is still performing well after more than four years in orbit, with a noise level of $200\,pm/\sqrt{Hz}$ at Fourier frequencies of 1 Hz (Abich et al., 2019), 5000 times more precise than the KBR.

*Corresponding author:
Email address:* malte.misfeldt@aei.mpg.de (Malte Misfeldt)

Data processing of the inter-satellite range rate observations from KBR or LRI in addition to observations from the Global Positioning System (GPS) receivers, accelerometers, and star cameras as well as precise modeling of the ocean and solid Earth tides and other known effects yields monthly gravity maps of the Earth as the main scientific mission results (Wahr et al., 2004; Tapley et al., 2004). Comparing individual months and the long-term mean gravity reveals trends and annual hydrological signals for climate studies, such as accelerated ice sheet melting, groundwater storage depletion, closure of the sea-level rise budget, and more (Tapley et al., 2019). The successful commissioning of the LRI instrument was an essential step towards the Laser Interferometer Space Antenna (LISA) mission, which will use comparable inter-satellite laser ranging technology between three spacecraft in deep space for the detection of gravitational waves (Amaro-Seoane et al., 2017).

In this paper, we investigate the ranging data of the LRI for so-called Single Event Upsets (SEUs), which are short-lived disturbances in the phase measurement due to the interaction of charged particles or cosmic radiation with the onboard electronics. Section 2 discusses the space environment in the polar low-earth orbit and introduces different classifications of radiation effects on electronics. The LRI architecture is explained in section 3 with special attention on the Laser Ranging Processor (LRP), in which the SEUs occur. We simulate the digital filtering chain within the LRP in section 4 and create templates, which are then used to detect actual SEUs in the measured phase data in section 5. The identified SEUs are discussed in section 6, and the results are summarized and concluded in section 7.

2. Space Environment

The space radiation environment affects the electronics aboard spacecraft. Therefore space electronics are usually shielded or hardened against this radiation (Stassinopoulos & Raymond, 1988). The space environment encountered by the spacecraft is influenced by Earth's magnetic field and sources from outer space. The radiation effects from the sun are char-

acterized by its 11-year cycle, during which the sun emits a stream of particles with varying flux called the solar wind. It consists of electrons, protons, and heavy ions (Nwankwo et al., 2020). Galactic cosmic rays are another source of particle flux composed of high-energy protons. They originate outside the solar system, from the depths of our galaxy (Blasi, 2013). The Earth's magnetic field traps these charged particles, and they follow the magnetic field lines (Van Allen, 1959). Depending on the species of particles, they populate different regions of the magnetic field, like the Van Allen radiation belts (Bosser, 2017). It is a system of two concentric belts ranging from approximately 1000 km to over 60 000 km in altitude (Métrailler et al., 2019).

The probability for radiation-related incidents in space electronics is related to spatial variations of Earth's magnetic field. Over the past years, in-situ measurements were performed by several space missions and combined in the so-called CHAOS model (named after the space missions CHAMP, Ørsted, and SAC-C, Olsen et al. (2006)). The currently available version 7 of the CHAOS model also includes the SWARM mission results and ground data (Finlay et al., 2020). The region over the southern Atlantic exhibits a low magnetic field intensity at the altitude of a Low Earth Orbit (LEO), which is commonly called the South-Atlantic Anomaly (SAA). Here, the inner Van Allen belt approaches Earth's surface. Like GRACE-FO, satellites in a LEO orbit usually fly below the belt but may pass through the SAA. It is known for its high radiation levels and is the site of frequent radiation-related events on satellite electronics. One such effect are SEUs, occurring within the SAA region in roughly 50% of the total cases (Zhang et al., 2021).

When a single charged particle interacts with an electronic component like a transistor, it leaves a trail of electron-hole pairs within the semiconductor that generate a current pulse (Todd & Uznanski, 2015). This interaction either causes a hard error or a soft error: Hard errors cause severe malfunction up to defect of the device, while soft errors are temporary and nondestructive. Hence, SEUs are soft errors. They may influence the value of the bit stored by a memory cell (Todd & Uznanski,

2015). This bitflip prevails until a new bit value is passed into the memory cell. On the other hand, a Single Event Latchup (SEL) is a hard error that short circuits the electronics and can be disastrous (Rivetta et al., 2001). The GRACE satellite, the predecessor to GRACE-FO, experienced failure of one of the Instrument Control Units onboard one of its spacecraft in 2002, which is possibly deemed as the result of a SEL (Pritchard et al., 2002).

3. LRI Architecture

The LRI is a single instrument distributed on two equally equipped spacecraft, called GF-1 and GF-2, and it measures the biased range between the spacecraft. It is operated in an active-transponder configuration (Sheard et al., 2012): One of the two units (the reference unit) sends out a laser beam with approx. 25 mW optical power, which is stabilized to a reference cavity using the Pound-Drever-Hall technique (Drever et al., 1983; Thompson et al., 2011). The frequency of the emitted light field appears Doppler shifted by a frequency $f_D < 3$ MHz due to the relative motion of the two spacecraft when it is sensed on the distant transponder spacecraft (Sheard et al., 2012). On the transponder unit, the incoming beam has only pico- to nanowatts of optical power due to the divergence of Gaussian beams and a small aperture at reception. The transponder laser is controlled by a feedback loop such that the incoming beam is reproduced with a well-defined phase relation but amplified in power before being sent back to the reference spacecraft. The transponder unit also intentionally introduces a frequency offset of $f_{off} = 10$ MHz. A second Doppler shift on the way back is sensed on the reference spacecraft. Ultimately, the interference between the local oscillator and round-trip beams is measured on the reference side and reads $f_R = 2f_D + f_{off}$ in terms of the beat frequency. Since the frequency offset f_{off} is known, range and gravity information in the form of Doppler shifts f_D can be extracted from the measured frequency f_R. The LRI on the transponder spacecraft, in principle, measures zero phase variations except for a well-defined phase ramp, due to the afore mentioned feedback loop implementing the frequency offset.

Within the LRI, the main computing engine is called the LRP, which was built by Jet Propulsion Laboratory (JPL) (Bachman et al., 2017). It hosts the phase readout electronics alongside control loops for the laser, cavity, steering mirror and more. In this article, we focus on the data acquisition and processing chain, which we assume to function as depicted in figure 1. The phase of the interfering light on both spacecraft is sensed by a Quadrant Photodiode (QPD) allowing to retrieve ranging and beam tilt information (Sheard et al., 2012) from the four phase channels per spacecraft. The photocurrents are converted into voltages within the optical bench electronics and digitized at a rate of approximately 40 MHz before the phase information is extracted using an all-digital phase-locked loop within the LRP, see e. g. (Ware et al., 2006; Wand et al., 2006). The nominal clock rates of the digitization are 38.656 000 MHz for GF-1 and 38.656 792 MHz for GF-2. The phase extraction is divided between an FPGA, where an IQ-demodulation, filtering and decimation to 9.664 kHz is performed (9.664 198 kHz on GF-2), and a processor, which extracts the ranging phase $\varphi = \arctan(I/Q)$, which is further decimated in a 2-step low-pass-filtering and decimation chain. The whole phase extraction and decimation chain runs individually on each of the four phase channels on both spacecraft. The decimation in the processor comprises two FIR filters (A and B of length l_A and l_B) and two decimators by a factor of 100 and 10, respectively, to derive the final data rate of 9.664 Hz (9.664 198 Hz on GF-2), at which the phase data is transmitted to ground. Filtering before decimation is needed to prevent aliasing (Ware et al., 2006) of higher frequencies into the measurement band of 2 mHz to 0.1 Hz (Dahl et al., 2017). The two filters A and B each constitute some hundred registers (labelled m) and corresponding filter coefficients (Ware et al., 2006) with $l_A > l_B$. The filter coefficients $c_{A/B}$ contain the impulse response of such a filter. The phase delay of all three filters adds up, giving a combined filter delay of 28 802 038 clock ticks ≈ 0.745 s (Wen et al., 2019). After discussions with the JPL, the manufacturer of the LRP, we identify the two FIR filters A and B in the processor as the most probable source for radiation-induced SEUs because
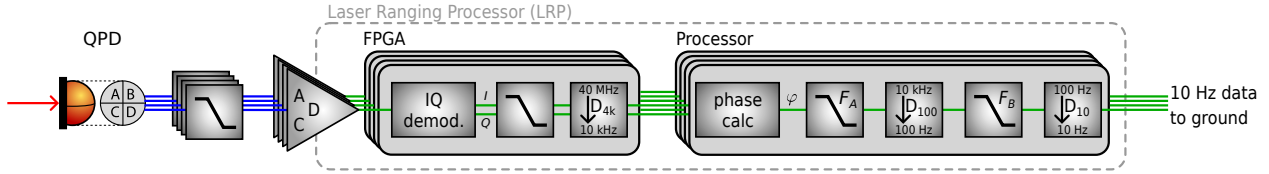
Fig. 1. Phasemeter processing chain. The optical signal is converted to a voltage by the QPD and its electronics. The voltage is filtered and digitized at a rate of approximately 40 MHz before the FPGA, which demodulates the signal. The phase is extracted in the processor, where further filtering and decimation takes place as well. The low-pass FIR filters in the processor are of length l_A and l_B, respectively, and the subsequent decimations are by a factor of 100 and 10. All shown elements are implemented independently for the four phase channels on each spacecraft. Red lines denote optical signals, blue is analog electronic and green are digital signals.

the FPGA can be expected to be better hardened against radiation than the memory of the processor and currently available space-qualified FPGAs even feature error detection and correction implemented in the hardware, see e. g., the RTG4 FPGA Series (Microchip Technology Inc., 2022).

In the following, we will use approximate values for the frequencies (e. g. 40 MHz instead of 38.656 MHz) in the text and sketches for brevity, while the simulations and data analysis uses the exact values.

4. Simulation of Events

In a time-domain simulation, the output of the FIR filtering chain was computed. A block diagram of the simulation is shown in figure 2. The filter response at a single time step is given by the sum over all the products of the register values m_i, containing the data φ, and their corresponding filter coefficients $c_{A/B}^i$. For the next time step, the registers values are shifted one sample to the right, and the register m_0 receives a new value from the input phase data.

We simulate the effect of SEU-induced bitflips with a trivial filter input being $\varphi \equiv 0$, i. e., without any ranging signal, in order to obtain just the disturbance from a bitflip, and we assume that this disturbance adds to the regularly filtered signal due to linearity of FIR filters. Hence, upon a bitflip, we set the m-th register from 0 to 1 during execution of the simulation. If the SEU occurs in filter A, it will then propagate through the subsequent filter and decimation stages. Manipulation of the 0th register in filter A is equivalent to setting one sample of the input phase φ to one. However, manipulation of higher registers can not be replaced by equivalent input data φ. All intermediate

data streams are computed, where F_A denotes the output of the first filter, which is then decimated by a factor of 100 (denoted D_{100}). The second filter output is F_B, and its decimated outcome at a 10 Hz data rate is called D_{10}.

We identified the defining parameters of a bitflip to be

- The affected filter (A or B).

- The occurrence time of the SEU, expressed as a sample number or tick $k_{A/B}$ at the filter's clock rate. Due to the fixed decimation rates from F_A or F_B to the 10 Hz output data rate ($1000 = 100 \cdot 10$ or 10, respectively), the output of a varying k repeats. Thus, if the SEU occurs in filter A we use $k_A \in [0, 1000) \subseteq \mathbb{N}_0$ and for an SEU in filter B we use $k_B \in [0, 10) \subseteq \mathbb{N}_0$. Now, k can be regarded as the subsample time in between of two data samples of the 10 Hz output data.

- The affected register number $m_A \in [0, l_A) \subseteq \mathbb{N}_0$ or $m_B \in [0, l_B) \subseteq \mathbb{N}_0$ of the filter. We usually provide this number in % of the full filter length $l_{A/B}$.

- The bit number $b \in [0, 64) \subseteq \mathbb{N}_0$ that flipped of the presumed 64-bit register (i. e. the 2^b magnitude of the flipped bit). For simulation, $b = 0$ is usually used, since this parameter is a linear scale factor that can easily be estimated through a least squares algorithm.

We simulate the bitflips with $\varphi = 0$ as initial condition and the bit flipping from zero to one. However, one could also initialize $\varphi = 1$ and flip from one to zero. This results in the same shapes of the output data but with inverted sign. Figure 3 shows an exemplary simulation result for an SEU in the first register ($m =$
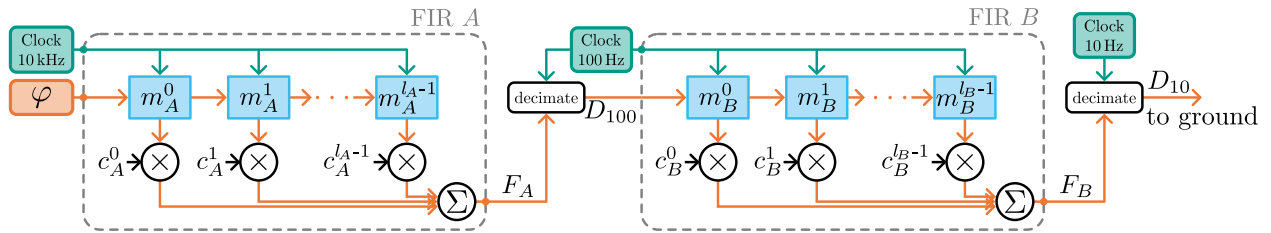
Fig. 2. Block Diagram of the two FIR filter stages as implemented for the simulation. Green denotes clock signals, orange denotes the phase data and blue denotes memory cells. The FIR filter coefficients ($c_{A/B}^i$) are multiplied with the data points in the registers and the filtered result is the sum over all multiplications.
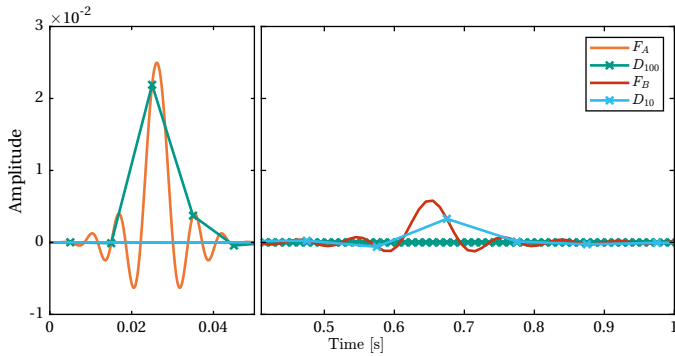

Fig. 3. Simulated data throughout the filtering chain for an SEU in the first FIR filter with injection sample and register number $k = m = 0$ and a magnitude $a = 1$. The input data φ is zero and thus not shown. The output of the first filter F_A (orange) is sampled at 10 kHz, the first decimation D_{100} (green) and the output of the second filter F_B (red) at 100 Hz and the final output D_{10} (cyan) is sampled at 10 Hz. Both time-axes are in units of seconds, but note the different scale. These examples show artificial filter coefficients, as the exact coefficients employed in-flight can unfortunately not be disclosed here.
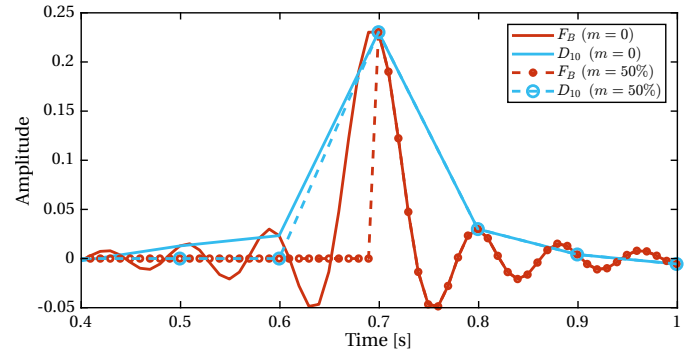

Fig. 4. Simulated data showing the effect of an SEU in a higher register number for the second filter. The solid lines depict the response of an impulse travelling through the full filter (i. e., for $m = 0$), while the dashed lines show the response for an SEU that affects the register $m = 50\%$ in the middle of the filter. Color coding as in figure 3. Note, that the magnitude here is larger than in figure 3, because this SEU was simulated in the second instead of the first FIR filter. These examples show artificial filter coefficients, as the exact coefficients employed in-flight can unfortunately not be disclosed here.

0) of the first filter (A) at time $k_A = 0$. Orange and green are the intermediate data streams after the first filter, red is the second filter's output, and cyan is the final 10 Hz output data. A larger injection sample, $k_A > 0$, would cause a delay of F_A and thus a slightly different shape and amplitude of the subsequent data streams due to the different sampling of F_B.

When a low register number m is affected by the bitflip it implies that almost the complete filter impulse response is visible in the immediate output, as shown by the solid lines of figure 4, where the red line depicts the immediate output of filter B at 100 Hz and blue denotes the decimated data at 10 Hz. A higher register number m yields cropped filter responses in the immediate output, as shown by the dashed lines in figure 4. For a high register number m in filter A, the 10 Hz output data would not appear cropped since the cropped and decimated filter output D_{100} is filtered once more in F_B, which ultimately dominates the shape of the output D_{10}.

For a fixed register number m, the output D_{10} can have very different shapes, depending on the time or sample k at which the SEU was induced in the data. There are 1000 unique patterns in the 10 Hz output data stream for an SEU in the first filter A and ten patterns for the second filter B, according to the sampling rate decimation factors. The ten patterns of filter B are approximately a subset of the 1000 patterns of filter A since the output D_{100} of filter A is approximately only a single peak which is then fed into filter B.

Two Look-Up Tables (LUTs) for events either in filter A or B were created from the simulations, where the injection sample number k and the register number m at which the SEU was injected into the filter were varied over the parameter space. The resulting output data after the second decimation, i. e., at 10 Hz, is stored in the LUTs. The full 3D-LUTs have the dimensions $1000 \times l_A \times 15$ and $10 \times l_B \times 15$, respectively, where the first dimension represents the injection sample number k, the second

dimension is the register number m and the third dimension is the total number of data points of the complete filter response at 10 Hz in D_{10}. The individual rows of the LUTs are denoted as $\text{LUT}_{A/B}^{k,m}$. For better readability, we will omit the subscript A/B in the following, where we usually mean that all the equations are evaluated independently for both LUTs.

Since the true LRP-internal filter coefficients are only available project-internally, we use exemplary FIR filters to show the principle in figures 3 and 4. The following analysis of actual flight-data however uses the true in-flight LRP filter coefficients.

5. Detection of SEUs in LRI Phase Data

The SEU detection algorithm is part of a larger framework developed at the Albert-Einstein-Institute in Hanover to automatically process and analyze LRI data in near-real-time (Misfeldt, 2019). It features an outlier-detection, originally developed to remove thruster-induced phase jumps (Abich et al., 2019) but was now extended to identify SEUs. The overall process is two-fold: first, all phase disturbance events are detected and categorized. All events where the first derivative of the measured phase (or the phase rate) exhibits steps larger than ± 30 mHz, or where the Differential Wavefront Sensing (DWS) combination shows outliers larger than 2×10^{-4} cycles/s, are marked as potential phase disturbance events. Subsequently, modeling and subtraction are performed. The criterion for deciding whether a phase disturbance is an SEU and not a true phase jump due to optical or mechanical disturbances is that an SEU occurs in a single channel only since the filtering and decimation of the four channels are performed separately. In contrast, a phase jump affects all four channels, and further, an SEU produces a short-lived peak (after propagating through the filter, the disturbance vanishes), while a phase jump causes a persistent step in the ranging data (caused by a non-zero integral of fast laser frequency variations, cf. Misfeldt (2019)). A short segment of $N \leq 30$ samples of the affected channel is extracted from the measured phase data once an SEU candidate is identified. The mean over the three unaf-

fected channels is subtracted from the affected channel to remove the common (ranging) signal and extract a clean signature of the SEU. We call this extracted bitflip signal $\varphi(t_i)$ or φ_i, where t_i are the discrete-time samples and i is the sample number. Exemplarily, if an SEU occurs in channel C, then $\varphi(t_i) = \varphi_C(t_i) - (\varphi_A(t_i) + \varphi_B(t_i) + \varphi_D(t_i))/3$. This expression additionally suppresses common-mode noises like laser frequency noise (on the reference side). The measurement noise of the LRI is discussed in more detail in Müller et al. (2022).

We introduce our model for the SEU phase

$$\eta_i^{k,m}(a) = \eta^{k,m}(a, t_i) = a \cdot \text{LUT}^{k,m}(t_i)\,, \quad (1)$$

which essentially is an LUT entry scaled by an amplitude a, and the residuals

$$\begin{aligned} r_i^{k,m}(\boldsymbol{\vartheta}) &= r\left((a, c_2, c_1, c_0)^\mathsf{T}, t_i\right) \\ &= \varphi_i - \eta_i^{k,m}(a) - c_2 \cdot t_i^2 - c_1 \cdot t_i - c_0\,, \quad (2) \end{aligned}$$

where we further subtract a second order polynomial, which may still be present in the data φ due to insufficient (ranging) signal removal or similar effects. This equation defines the regression coefficients $\boldsymbol{\vartheta} = (a, c_2, c_1, c_0)^\mathsf{T}$.

To assess which of the $k \times m$ models in the LUTs matches the data best, we employ the framework of maximum likelihood estimation. First, we compute the likelihood of $\boldsymbol{\vartheta}$ given the measured data φ as (Koch, 1999)

$$\mathcal{L}^{k,m}(\varphi \,|\, \boldsymbol{\vartheta}) = \frac{1}{\sqrt{|2\pi\Sigma|}} \cdot \exp\left(-\frac{1}{2} r^{k,m}(\boldsymbol{\vartheta})^\mathsf{T} \, \Sigma^{-1} \, r^{k,m}(\boldsymbol{\vartheta})\right)\,. \quad (3)$$

The covariance matrix Σ will be discussed later. The best fitting model $\eta^{k,m}(a)$ can be identified by the maximum value of the likelihood function $\mathcal{L}$ over the parameter space or equivalently by the minimum of its negative logarithm

$$\ell^{k,m}(\varphi \,|\, \boldsymbol{\vartheta}) = -\ln \mathcal{L}^{k,m}(\varphi \,|\, \boldsymbol{\vartheta}) \quad (4)$$

$$= \frac{1}{2} \ln\left(|2\pi\Sigma|\right) + \frac{1}{2} r^{k,m}(\boldsymbol{\vartheta})^\mathsf{T} \cdot \Sigma^{-1} \cdot r^{k,m}(\boldsymbol{\vartheta})\,. \quad (5)$$

The parameter space is discrete for the parameters k and m and continuous for $\boldsymbol{\vartheta}$. Hence we minimize the negative log-likelihood $\ell^{k,m}$ for all k, m through a generalized least squares,
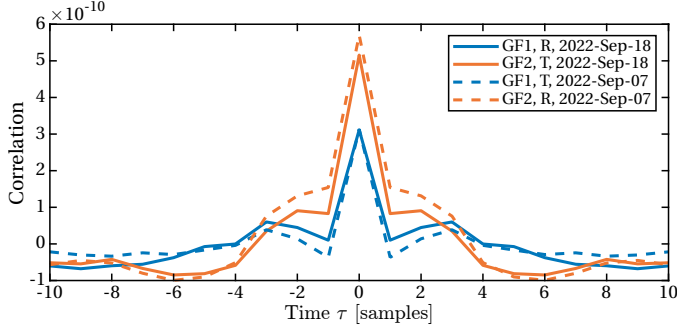
Fig. 5. Exemplary autocorrelation for a single channel phase combination $\varphi_A - (\varphi_B + \varphi_C + \varphi_D)/3$ of GF-1 and GF-2 on two different days with different roles.
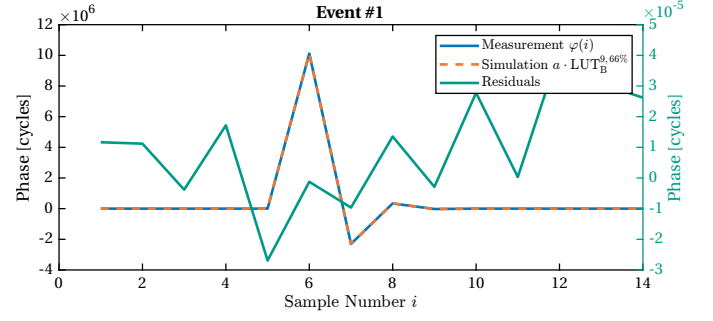

Fig. 6. Event #1: Example of a good SEU fitting result. The blue trace shows the isolated segment from the phase data of channel D on GF-2 on 2018-July-09 around 18:25 UTC. An SEU in bit $b = 60$ of the register $67\% \cdot l_B$ of the filter B (dashed orange) was subtracted, which yields the green residuals (scale according to right axis). The noise after subtraction is in the order of 10^{-5} cycles.

i. e., by estimating

$$\hat{\boldsymbol{\vartheta}} = \underset{\boldsymbol{\vartheta}}{\text{argmin}}\ r^{k,m}(\boldsymbol{\vartheta})^\top \cdot \Sigma^{-1} \cdot r^{k,m}(\boldsymbol{\vartheta})\ . \tag{6}$$

Ultimately, the best estimate for the SEU model is determined by finding the minimum of $\ell^{k,m}(\varphi\,|\,\hat{\boldsymbol{\vartheta}})$ in the two-dimensional $k \times m$-sized grid.

The covariance matrix Σ, which is needed to compute the generalized least squares (cf. equation (6)), is derived from the expectation value E of the measurement noise n as

$$\Sigma_{ij} = \mathrm{E}[n_i \cdot n_j] = R_n(t_i - t_j)\ . \tag{7}$$

Here, the expectation value E can be computed through the unbiased correlation function of the (real-valued) data n of length N as

$$R_n(\tau) = \begin{cases} \dfrac{1}{N-\tau} \displaystyle\sum_{i=0}^{N-\tau-1} n_{i+\tau} n_i\,, & \tau \geq 0 \\[2mm] R_n(-\tau)\,, & \tau < 0\,. \end{cases} \tag{8}$$

The correlation function is obtained from the autocorrelation of actual phase data in absence of an SEU event. Shown in figure 5 is the mean over 20 000 autocorrelations of consecutive data segments with 30 samples length for the two spacecraft in both roles. A trend was removed from the phase data before computing each autocorrelation. The function differs a bit in their shape between GF-1 and GF-2, and the magnitude varies insignificantly between different days in different roles (reference or transponder). The values of the solid lines are used as the correlation function $R_n(\tau)$ to form the covariance matrix Σ from the measurement noise n.

From the fitted amplitudes a of the LUT rows, we directly obtain the amplitude and sign of the SEU as it occurred before

the filtering. We can further compute the bit number b of the affected bit by

$$b = \log_2\left(10 \cdot 2^{24} \cdot a\right)\,, \tag{9}$$

where $1/(10 \cdot 2^{24})$ is the least significant bit in units of phase cycles in the LRI phase measurement (Wen et al., 2019). Ideally, b yields an integer number.

The above computation is done individually for all templates in the two filter's LUTs ($\mathrm{LUT}_A^{k,m}$ and $\mathrm{LUT}_B^{k,m}$). We compare the two minimal values of the log-likelihood over the LUTs to identify the most likely filter (A or B) when the SEU occurred.

6. Discussion

Over the analyzed mission time ranging from June 2018 until the end of December 2022, in which the LRI was in science mode for more than 75% of the time, we identified 29 SEU events in the LRI phase data, whose parameters are shown in table 1. A time series of an exemplary SEU event (#1 in the table), the fitted model, and the corresponding residuals are shown in figure 6.

Of all events, GF-1 recorded 14 events, while GF-2 recorded 15 events. As the reference/transponder role can be switched, 16 were detected on the transponder unit, and 13 on the reference unit of the LRI. The distribution over the four channels is almost equal (A: 8 events, B: 6, C: 8, D: 7). Filter A shows more events (19 vs. 10 in filter B). This is expected, since filter A has more registers $l_A > l_B$, i. e., a physically larger area in the electronics that can be hit by radiation. Given that the LRI was

in science mode for more than 85% of the time in 2019–2021, approximately nine events can be expected annually. It was not in science mode for long periods in 2018 and 2022; thus, fewer events were observed. The smallest observed event occurred in the 29th bit (event #28). Thus we expect that there are actually more SEU events at low bit numbers, but they are not detectable in the LRI noise.

The subtraction of the SEU signature from ranging data, in general, works well since the rms of the residuals is in the order of some 10^{-5} cycles in most of the cases, which is the noise level of the phase measurement system (cf. Müller et al. (2022)).

The distribution of the ground-track position of the spacecraft at the time of the SEU events (shown in figure 7) reveals an expected clustering within the South-Atlantic Anomaly, where almost 50% of the events take place. This is consistent with results from the literature (Zhang et al., 2021).

We did explicitly exclude the possibility, that an SEU could also alter the filter coefficients. A bitflip in the coefficients would cause a different filter gain and noise suppression. However, the exact effects also strongly depend on the architecture and implementation in the LRP.

Table 1. SEU parameters as detected in the LRI phase data. Ch denotes the affected phase channel; k is the sub-sample timing of the event; m is the affected register (normalized by the total number of registers $l_{A/B}$); b is the bit that flipped; Dir denotes the direction of the bitflip ($0 \rightarrow 1$ ($\uparrow$) or $1 \rightarrow 0$ ($\downarrow$). A 95% confidence interval (CI) for the bit number, derived from the formal errors of the least squares fit and assuming a Gaussian distribution, is computed as 1.96 times the standard deviation of the noise. The colored bit position cells are encoded as follows: Green: Fractional number can be well explained with two bitflips at the same time. Yellow: Fractional number can possibly be explained with more than two bitflips at the same time. Gray: High residuals observed (see main text, section 6.2). The horizontal lines separate different years.

| #	Event Time [UTC]	SC	Role	Ch	FIR	k	m [%]	Dir	Bit No. b int+frac	95% CI Bit No. b	Residuals [cycles rms]
1	09-Jul-2018 18:25:01	GF-1	T	D	B	9	66	↑	$60 + 1.25 \times 10^{-12}$	$\pm 4.29 \times 10^{-12}$	1.33×10^{-5}
2	20-Jan-2019 09:31:55	GF-1	R	D	A	296	31	↑	35 -1.97e-02	$\pm 1.49 \times 10^{-4}$	9.09×10^{-6}
3	01-Apr-2019 16:36:27	GF-2	T	B	A	352	0	↓	$46 - 2.73 \times 10^{-4}$	$\pm 6.20 \times 10^{-4}$	7.42e-02
4	18-Apr-2019 23:38:38	GF-2	T	C	A	165	37	↑	$63 + 8.81 \times 10^{-13}$	$\pm 2.13 \times 10^{-12}$	2.53×10^{-5}
5	09-Sep-2019 00:07:28	GF-2	T	A	B	4	6	↓	30 8.75e-02	$\pm 3.59 \times 10^{-5}$	7.36×10^{-6}
6	13-Nov-2019 23:31:24	GF-1	R	D	A	316	67	↓	53 2.12e-01	$\pm 2.43 \times 10^{-8}$	1.03×10^{-5}
7	20-Nov-2019 03:09:38	GF-1	R	A	A	309	49	↓	$50 + 6.70 \times 10^{-8}$	$\pm 1.07 \times 10^{-7}$	1.11×10^{-5}
8	25-Nov-2019 15:30:17	GF-1	R	C	B	1	65	↓	$34 - 8.10 \times 10^{-5}$	$\pm 3.59 \times 10^{-4}$	8.39×10^{-6}
9	06-Jan-2020 06:13:57	GF-2	T	C	B	4	56	↓	$41 + 1.33 \times 10^{-1}$	$\pm 4.87 \times 10^{-3}$	1.71e-01
10	01-Feb-2020 16:24:25	GF-2	T	A	A	299	31	↑	33 -1.59e-01	$\pm 4.42 \times 10^{-4}$	5.66×10^{-6}
11	22-Mar-2020 00:51:54	GF-1	R	A	A	797	51	↑	35 -1.51e-01	$\pm 1.46 \times 10^{-2}$	3.88×10^{-5}
12	01-May-2020 08:07:03	GF-1	R	C	A	646	0	↓	32 -9.28e-04	$\pm 1.35 \times 10^{-3}$	1.06×10^{-5}
13	30-May-2020 09:31:44	GF-1	R	A	A	394	32	↓	$59 + 2.92 \times 10^{-12}$	$\pm 1.18 \times 10^{-11}$	1.06×10^{-5}
14	17-Aug-2020 23:27:50	GF-1	R	A	B	1	86	↑	39 2.56e-01	$\pm 2.54 \times 10^{-3}$	8.27×10^{-6}
15	07-Sep-2020 01:47:43	GF-2	T	A	B	6	0	↑	$37 - 4.50 \times 10^{-2}$	$\pm 1.09 \times 10^{-6}$	2.35×10^{-5}
16	12-Sep-2020 02:17:38	GF-1	R	B	A	974	16	↑	29 -1.12e-02	$\pm 8.84 \times 10^{-3}$	8.89×10^{-6}
17	11-Dec-2020 18:06:47	GF-2	T	D	A	903	30	↑	49 -6.70e-09	$\pm 7.84 \times 10^{-9}$	9.22×10^{-6}
18	19-Dec-2020 04:44:29	GF-2	T	B	A	370	76	↓	54 2.73e-01	$\pm 8.71 \times 10^{-9}$	7.46×10^{-6}
19	09-Mar-2021 11:18:40	GF-2	T	D	B	3	35	↓	$51 + 1.23 \times 10^{-11}$	$\pm 3.96 \times 10^{-11}$	1.61×10^{-5}
20	10-Mar-2021 18:20:28	GF-2	T	D	A	218	47	↓	$39 + 8.81 \times 10^{-5}$	$\pm 8.57 \times 10^{-5}$	1.22×10^{-5}
21	12-Mar-2021 23:20:11	GF-2	R	C	A	434	24	↑	37 -3.24e-04	$\pm 2.90 \times 10^{-5}$	8.18×10^{-6}
22	25-Jul-2021 00:27:50	GF-2	T	B	B	0	23	↑	$51 + 8.50 \times 10^{-11}$	$\pm 6.20 \times 10^{-11}$	2.58×10^{-5}
23	30-Sep-2021 19:46:16	GF-2	T	A	A	57	0	↑	$44 - 3.39 \times 10^{-8}$	$\pm 5.13 \times 10^{-7}$	2.13×10^{-5}
24	16-Nov-2021 16:25:26	GF-2	T	C	A	18	7	↓	$45 + 1.53 \times 10^{-7}$	$\pm 3.65 \times 10^{-7}$	2.23×10^{-5}
25	05-Dec-2021 04:06:04	GF-1	R	C	A	454	60	↑	38 -3.05e-02	$\pm 3.05 \times 10^{-4}$	9.73×10^{-6}
26	27-Jan-2022 22:21:58	GF-1	R	B	B	7	32	↓	$51 - 1.75 \times 10^{-11}$	$\pm 1.84 \times 10^{-11}$	7.06×10^{-6}
27	04-Jun-2022 15:21:35	GF-1	T	D	A	721	46	↑	$63 - 3.03 \times 10^{-12}$	$\pm 3.70 \times 10^{-12}$	1.09×10^{-5}
28	07-Nov-2022 12:32:14	GF-1	R	C	B	9	66	↓	29 8.51e-03	$\pm 1.20 \times 10^{-2}$	1.91×10^{-5}
29	22-Nov-2022 22:27:29	GF-2	T	B	A	542	2	↑	$63 + 3.34 \times 10^{-13}$	$\pm 1.23 \times 10^{-12}$	1.96×10^{-5}
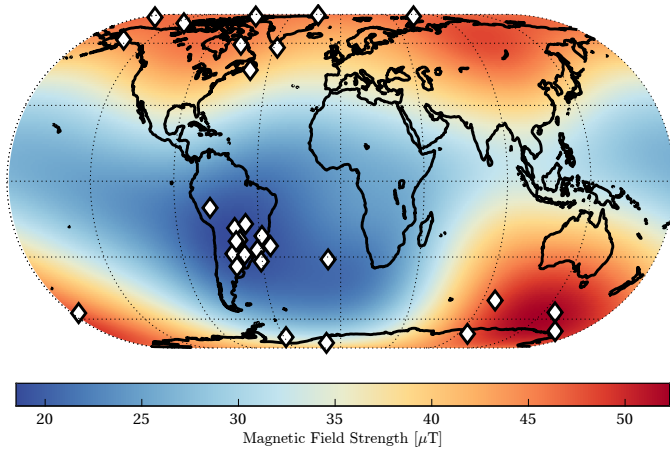
Fig. 7. World map showing the location of the GRACE-FO spacecraft at occurrence of SEUs (diamonds). The color coding depicts the strength of the magnetic field in μT at an altitude of 490 km above Earth's surface, as derived from the CHAOS-7 model for January 2021 (Finlay et al., 2020). There is evidence for an increased number of SEUs in the region of the South-Atlantic Anomaly.

Table 2. Fractional bit number for two bitflips at the same time as a function of the separation between bit numbers. The number n denotes position $b - n$ of the second bit, relative to the one at position b, $b > n$.

n	$O_+(n)$	$O_-(n)$
1	0.58496	-1
2	0.32193	-0.41504
3	0.16993	-0.19265
4	0.08746	-0.09311
5	0.04439	-0.04580
6	0.02237	-0.02272
7	0.01123	-0.01131
8	0.00562	-0.00565
9	0.00282	-0.00282
10	0.00141	-0.00141
11	0.00070	-0.00070
12	0.00035	-0.00035
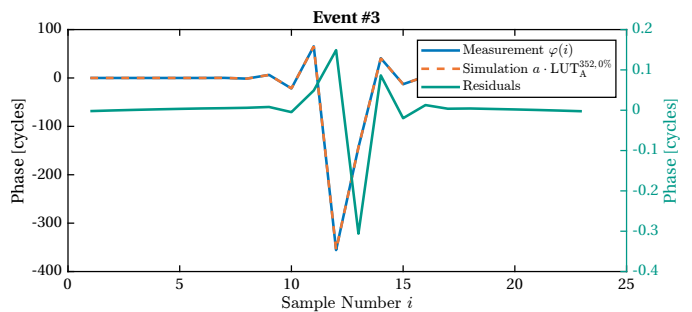
Fig. 8. Event #3: The residuals are shaped like a second SEU.

6.1. Non-Integer Bit Numbers

Some events show bit number b, that are not integer within the 95% confidence interval, marked with different colors in table 1. Though non-integer bit numbers seem contra-intuitive in the first place, it can be explained when considering a simultaneous bitflip in separate bits. This increases or decreases the signal's amplitude and thus the retrieved bit number b (cf. equation (9)). The allowed fractional bit numbers obtained from our fit only depend on the separation in bits between the affected bits:

$$O_\pm(n) = \log_2(2^b \pm 2^{b-n}) - \log_2(2^b) . \qquad (10)$$

The sign of the 2^{b-n}-term denotes the direction of the lower bit at position $b-n$ with respect to the flip direction of the upper bit b, which is indicated in table 1. The first 12 allowed fractional bit values are shown in table 2. Note that $O_+(1)$ and $O_-(2)$ are degenerate and also a flip in bit b and $b-1$ in different directions can not be distinguished from a single flip in the $b-1$-th bit. Comparing the allowed fractional bit numbers from table 2 with the values in column "Bit No. b" of table 1, several events can be explained by multiple bitflips. For instance, we observe $O_+(4)$ (the 30th and 26th bit flipped in the same direction) for event #5. All these events are marked green. The numbers of table 2 can not directly explain the events marked yellow.

However, these fractional bit positions can be explained when considering even more than two bitflips simultaneously. The fractional bit number of event #10 is $-0.159 \approx O_-(3) + O_+(5)$, which denotes bitflips in the 31st, 28th and 26th bit. Any assessment of how likely a single particle's impact may induce two bits to flip strongly depends on the exact architecture and physical arrangement of the memory cells, which is unknown to the authors.

6.2. Other Events

There are two events where the residuals still show a comparatively large rms value (#3 and #9; marked gray). Their residuals look like another SEU event, separated from the initial one by a few milliseconds. Event #3 is exemplarily shown in figure 8. A short experiment of feeding these residuals again into the fitting algorithm did not succeed, likely because these two events lived simultaneously within the filter and can not be treated as a simple superposition of two independent events.

Extending the LUTs also to incorporate such events was beyond the scope of this study and would exponentially increase the size of the LUTs and the computation time.

7. Conclusion

In this paper, we presented an approach to identify, extract and model SEU-induced disturbances in the measured phase data of the LRI in the GRACE-FO mission. We explain the filtering within the LRP, where we expect SEUs to show an effect in the measured phase through flipped bits in the registers of the lowpass FIR filters. Further, we showed simulated data and discussed the parameters needed to describe the SEU. Ultimately, we found 29 events in more than three years of LRI ranging data. The events clustered at the South-Atlantic Anomaly. Some of the events seem to originate from multiple bits flipping simultaneously or possibly even with a slight time delay.

Radiation-induced SEU in the LRI phase data are rare and short-lived events. Thus, we expect that their non-removal has only little to none impact on the retrieved gravity fields. Nevertheless, LRI data products with removed SEUs can be found at https://www.aei.mpg.de/grace-fo-ranging-datasets.

This study shows that it is possible to identify and remove this particular noise source in post-processing. Future instruments might overcome this source of short measurement disturbances by implementing radiation-hardened memory or incorporating error correction algorithms.

References

Abich, K., Abramovici, A., Amparan, B. et al. (2019). In-orbit performance of the GRACE follow-on laser ranging interferometer. *Physical Review Letters*, *123*(3). doi:10.1103/physrevlett.123.031101.

Amaro-Seoane, P., Audley, H., Babak, S. et al. (2017). Laser interferometer space antenna. doi:10.48550/ARXIV.1702.00786.

Bachman, B., de Vine, G., Dickson, J. et al. (2017). Flight phasemeter on the laser ranging interferometer on the grace follow-on mission. *Journal of Physics: Conference Series*, *840*, 012011. doi:10.1088/1742-6596/840/1/012011.

Blasi, P. (2013). The origin of galactic cosmic rays. *The Astronomy and Astrophysics Review*, *21*(1). doi:10.1007/s00159-013-0070-7.

Bosser, A. (2017). *Single-event effects of space and atmospheric radiation on memory components*. Ph.D. thesis University of Jyväskylä. URL: http://urn.fi/URN:ISBN:978-951-39-7312-4.

Dahl, C., Baatzsch, A., Dehne, M. et al. (2017). Laser ranging interferometer on grace follow-on. In N. Karafolas, B. Cugny, & Z. Sodnik (Eds.), *International Conference on Space Optics — ICSO 2016*. SPIE. doi:10.1117/12.2297705.

Drever, R. W. P., Hall, J. L., Kowalski, F. V. et al. (1983). Laser phase and frequency stabilization using an optical resonator. *Applied Physics B*, *31*(2), 97–105. doi:10.1007/BF00702605.

Finlay, C. C., Kloss, C., Olsen, N. et al. (2020). The CHAOS-7 geomagnetic field model and observed changes in the south atlantic anomaly. *Earth, Planets and Space*, *72*(1), 156. doi:10.1186/s40623-020-01252-9.

Koch, K.-R. (1999). *Parameter Estimation and Hypothesis Testing in Linear Models*. Springer Berlin Heidelberg. doi:10.1007/978-3-662-03976-2.

Kornfeld, R. P., Arnold, B. W., Gross, M. A. et al. (2019). GRACE-FO: The Gravity Recovery and Climate Experiment Follow-On Mission. *Journal of Spacecraft and Rockets*, *56*(3), 931–951. doi:10.2514/1.A34326.

Microchip Technology Inc. (2022). RTG4™ Radiation-Tolerant FPGAs. URL: https://www.microchip.com/en-us/products/fpgas-and-plds/radiation-tolerant-fpgas/rtg4-radiation-tolerant-fpgas.

Misfeldt, M. (2019). *Data Processing and Investigations for the GRACE Follow-On Laser Ranging Interferometer*. Master's thesis Leibniz Universität Hannover. doi:10.15488/9639.

Métrailler, L., Bélanger, G., Kretschmar, P. et al. (2019). Data-driven modelling of the van allen belts: The 5drbm model for trapped electrons. *arXiv*, . doi:10.48550/ARXIV.1907.11029.

Müller, V., Hauk, M., Misfeldt, M. et al. (2022). Comparing GRACE-FO KBR and LRI ranging data with focus on carrier frequency variations. *Remote Sensing*, *14*(17), 4335. doi:10.3390/rs14174335.

Nwankwo, V. U.-J., Jibiri, N. N., & Kio, M. T. (2020). The impact of space radiation environment on satellites operation in near-earth space. In V. Demyanov, & J. Becedas (Eds.), *Satellites Missions and Technologies for Geosciences* chapter 5. Rijeka: IntechOpen. doi:10.5772/intechopen.90115.

Olsen, N., Lühr, H., Sabaka, T. J. et al. (2006). CHAOS-a model of the earth's magnetic field derived from CHAMP, Ørsted, and SAC-c magnetic satellite data. *Geophysical Journal International*, *166*(1), 67–75. doi:10.1111/j.1365-246x.2006.02959.x.

Pritchard, B., Swift, G., & Johnston, A. (2002). Radiation effects predicted, observed, and compared for spacecraft systems. In *IEEE Radiation Effects Data Workshop*. IEEE. doi:10.1109/redw.2002.1045525.

Rivetta, C., Allongue, B., Berger, G. et al. (2001). Single event burnout in DC-DC converters for the LHC experiments. In *RADECS 2001. 2001 6th European Conference on Radiation and Its Effects on Components and Systems (Cat. No.01TH8605)*. IEEE. doi:10.1109/radecs.2001.1159300.

Sheard, B. S., Heinzel, G., Danzmann, K. et al. (2012). Intersatellite laser ranging instrument for the GRACE follow-on mission. *Journal of Geodesy*, *86*(12), 1083–1095. doi:10.1007/s00190-012-0566-3.

Stassinopoulos, E., & Raymond, J. (1988). The space radiation environment for electronics. *Proceedings of the IEEE*, *76*(11), 1423–1442. doi:10.1109/5.90113.

Tapley, B. D., Bettadpur, S., Watkins, M. et al. (2004). The gravity recovery and climate experiment: Mission overview and early results. *Geophysical Research Letters*, *31*(9). doi:10.1029/2004GL019920.

Tapley, B. D., Watkins, M. M., Flechtner, F. et al. (2019). Contributions of GRACE to understanding climate change. *Nature Climate Change*, *9*(5), 358–369. doi:10.1038/s41558-019-0456-2.

Thompson, R., Folkner, W. M., de Vine, G. et al. (2011). A flight-like optical reference cavity for GRACE follow-on laser frequency stabilization. In *Joint Conference of the IEEE International Frequency Control and the European Frequency and Time Forum (FCS) Proceedings*. IEEE. doi:10.1109/fcs.2011.5977873.

Todd, B., & Uznanski, S. (2015). Radiation risks and mitigation in electronic systems. doi:10.5170/CERN-2015-003.245.

Van Allen, J. A. (1959). Radiation belts around the earth. *Scientific American*, *200*(3), 39–47. URL: http://www.jstor.org/stable/24944942.

Wahr, J., Molenaar, M., & Bryan, F. (1998). Time variability of the Earth's gravity field: Hydrological and oceanic effects and their possible detection using GRACE. *Journal of Geophysical Research: Solid Earth*, *103*(B12), 30205–30229. doi:10.1029/98JB02844.

Wahr, J., Swenson, S., Zlotnicki, V. et al. (2004). Time-variable gravity from GRACE: First results. *Geophysical Research Letters*, *31*(11). doi:10.1029/2004gl019779.

Wand, V., Guzmán, F., Heinzel, G. et al. (2006). LISA phasemeter development. In *AIP Conference Proceedings*. AIP. doi:10.1063/1.2405118.

Ware, B., Folkner, W., Shaddock, D. et al. (2006). Phase Measurement System for Inter-Spacecraft Laser Metrology. *Earth Science Technology Conference*, .

Wen, H. Y., Kruizinga, G., Paik, M. et al. (2019). *GRACE-FO Level-1 Data Product User Handbook*. Jet Propulsion Laboratory. URL: https://podaac-tools.jpl.nasa.gov/drive/files/allData/gracefo/docs/GRACE-FO_L1_Handbook.pdf JPL D-56935, Version of September 11, 2019.

Zhang, Y., Guo, D., Guo, K. et al. (2021). Analysis of single event upset on certain type of calibration satellite and research on the correlation characteristics. In Z. Zhang (Ed.), *2021 International Conference on Neural Networks, Information and Communication Engineering*. SPIE. doi:10.1117/12.2615276.